Materials Today Bio 32 (2025) 101697

Contents lists available at ScienceDirect

Materials Today Bio

journal homepage: www.journals.elsevier.com/materials-today-bio

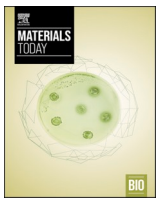

Novel pH-responsive lipid nanoparticles deliver UA-mediated mitophagy and ferroptosis for osteoarthritis treatment

Guoliang Yi [a,b], Min Li [a], Jiayi Zhou [a], Jinxin Li [a], Xizheng Song [a], Siming Li [b,c], Jianghua Liu [a,*], Haowei Zhang [a,**], Zhiwei Chen [a,***]

[a] Department of Orthopedics, The First Affiliated Hospital, Hengyang Medical School, University of South China, Hengyang, 421001, China
[b] Guizhou Medical University, Guiyang, 550004, China
[c] Department of Orthopedics, Guangzhou Red Cross Hospital, Guangzhou, 510220, China

ARTICLE INFO

Keywords:
Lipid nanoparticles
Urolithin A
Osteoarthritis

ABSTRACT

Synovial inflammation plays a crucial role in osteoarthritis (OA) development, leading to chronic inflammation and cartilage destruction. Although targeting synovitis can alleviate OA, clinical outcomes have been disappointing due to poor drug targeting and joint cavity heterogeneity. This study presents pH-responsive lipid nanoparticles (LNPs@UA), loaded with Urolithin A (UA), as a potential OA treatment. LNPs@UA showed uniform particle size, low zeta potential, and effective mitochondria-targeting and pH-responsive capabilities. In vitro, LNPs@UA reduced reactive oxygen species (ROS), pro-inflammatory factors (IL-1β, IL-6, TNF-α), and promoted M2 macrophage polarization. It improved mitochondrial structure, enhanced autophagy, and inhibited ferroptosis. In vivo, LNPs@UA alleviated OA progression in an ACLT-induced OA mouse model. Transcriptomic analysis revealed inhibition of NF-κB signaling and activation of repair pathways. These results suggest LNPs@UA could offer a promising therapeutic approach for OA.

1. Background

Osteoarthritis (OA) is a degenerative joint disorder characterized by inflammation that affects multiple synovial joints, leading to cartilage degradation, joint space narrowing, osteophyte formation, and synovitis. Synovial inflammation plays a pivotal role in OA pathogenesis by inducing pain and promoting articular cartilage degeneration and inflammation [1,2]. Current therapeutic options for OA include nonsteroidal anti-inflammatory drugs, intra-articular glucocorticoid and hyaluronic acid injections, mesenchymal stem cell therapy, and osteochondral transplantation [3]. However, clinical outcomes remain suboptimal, often necessitating eventual joint replacement owing to inadequate joint-specific drug delivery. Fortunately, advancements in nanomaterials offer promising avenues for targeted drug delivery and enhancing cartilage repair or regeneration through drug-loaded nanocarrier technologies. This innovation holds potential for identifying new therapeutic targets and improving treatment outcomes in OA patients.

Urolithin A (UA) is a metabolite derived from ellagic acid (EA) following intestinal processing, a process influenced by the gut microbiota, with only 40 % of individuals being capable of converting precursor molecules into UA [4,5]. As the most potent metabolite of EA, UA has notable anti-inflammatory properties [6]. Recent studies have highlighted its ability to inhibit inflammation [7], scavenge reactive oxygen species (ROS) [8], and enhance antioxidant enzyme activity [9]. Despite these beneficial effects, the potential use of UA for OA treatment remains unexplored [10], likely due to challenges such as low bioavailability and variable metabolic profiles among individuals. Encouragingly, advancements in liposome nanoparticles (LNPs) and microfluidic techniques offer potential solutions to these challenges. LNPs have been indicated as effective as drug carriers in clinical settings [11], offering advantages such as sustained release and improved drug stability. Moreover, LNPs can be tailored to enhance drug functionality through surface modifications [12]. Microfluidic technology, which involves precise manipulation of fluids at the micro- and nanoscales [13], enables the creation of drug-loaded liposome nanoparticles that are targeted, biocompatible, and uniformly sized [14–16]. These

* Corresponding author.
** Corresponding author.
*** Corresponding author.
E-mail addresses: jianghua_liu@163.com (J. Liu), 2018011172@usc.edu.cn (H. Zhang), czw9915@sina.com (Z. Chen).

https://doi.org/10.1016/j.mtbio.2025.101697
Received 14 October 2024; Received in revised form 10 March 2025; Accepted 20 March 2025
Available online 21 March 2025

advancements hold significant promise for OA treatment because they address issues related to drug delivery efficiency and effectiveness in targeting inflamed joints.

In this study, we developed novel pH-responsive lipid nanoparticles for the delivery of UA to treat OA. We have demonstrated that these nanoparticles offer distinct advantages for OA treatment in both in vitro and in vivo animal models. In OA, inflammation boosts repair but also causes cells to make lactic acid due to low oxygen, which acidifies the joint environment. In a healthy joint, synovial fluid has a pH of 7.4. However, as OA progresses and cartilage degrades, the pH gradually decreases to between 6.6 and 7.2, and can even drop to as low as 6.0 [17], which impedes effective drug delivery [18]. We designed LNPs encapsulating UA, modified with 2-(diisopropylamino) ethylamine (2-DIP) for pH-responsive drug release and triphenylphosphine (TPP) to target mitochondria. In OA, mitochondrial dysfunction and ROS accumulation play key roles in disease progression [19], and targeting

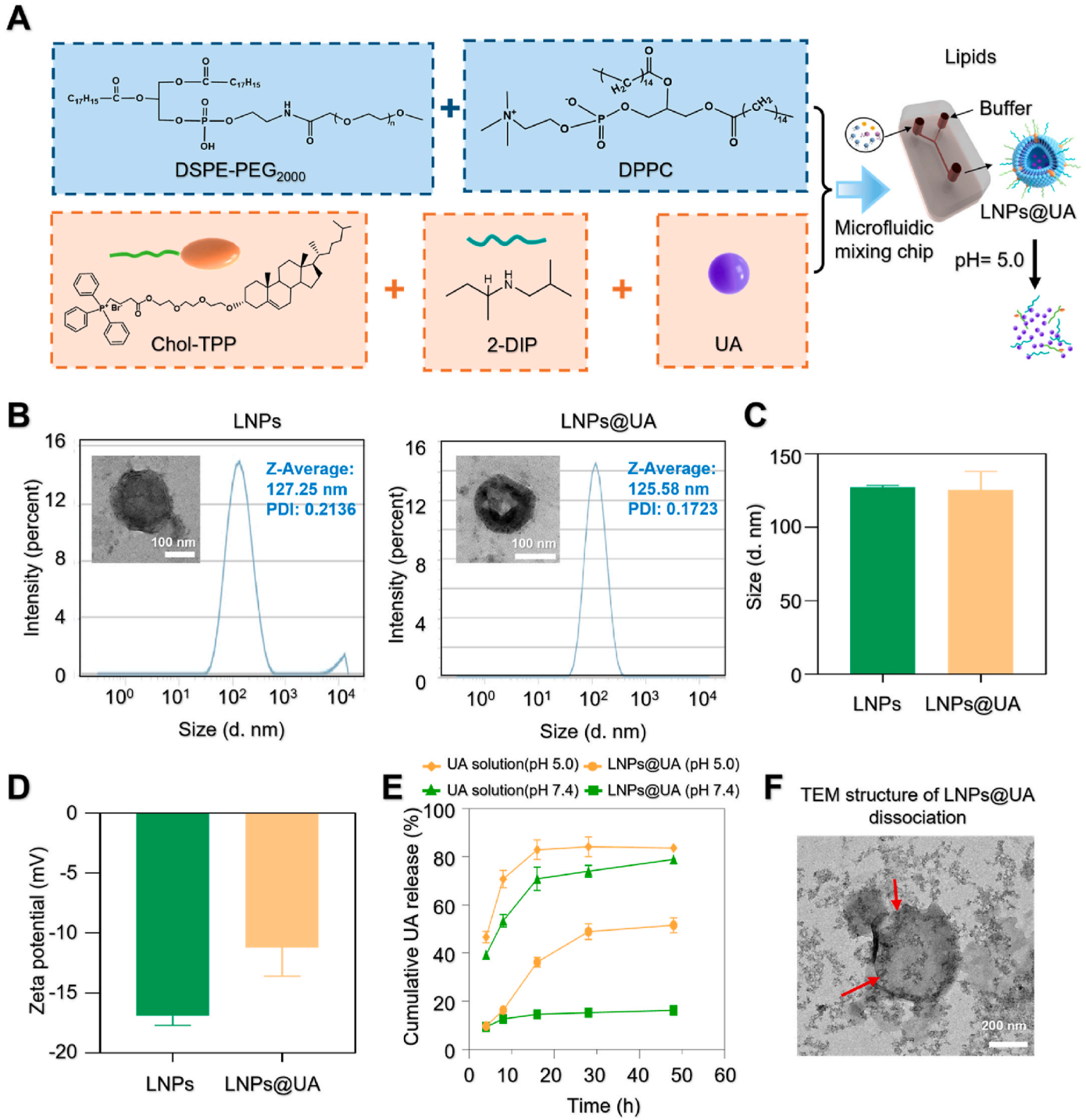

Fig. 1. Synthesis and characterization of LNPs@UA. (A) Schematic diagram illustrating the LNPs@UA preparation method. (B) Representative TEM images and particle sizes of LNPs and LNPs@UA. (C–D) Distribution of the particle size and zeta potential of LNPs and LNPs@UA, as detected by DLS (n = 3). (E) Release profiles of UA from LNPs@UA and pure UA solution under different pH conditions (n = 3). (F) Representative TEM image of LNPs@UA during the dissociation and release of UA.

mitochondria can help regulate the ROS-mitophagy-ferroptosis axis [20, 21]. Using microfluidic technology, we created UA-loaded LNPs that release UA in the acidic OA environment and selectively target mitochondria [22]. These nanoparticles reduce ROS levels, promote mitophagy, and inhibit ferroptosis, leading to reduced inflammation and cartilage damage. Additionally, LNPs@UA suppressed inflammatory cytokines and the NF-κB signaling pathway (see Graphical Abstract). The significance of this research lies in its potential to offer a new, effective strategy for treating OA. The LNPs@UA system holds promise for clinical application due to its stable, homogeneous physical properties, excellent biocompatibility, and in vivo safety. Overall, our study provides a promising approach to blocking OA progression by targeting mitochondria and modulating the OA microenvironment, offering substantial potential for future clinical use in OA treatment.

2. Methods

2.1. Synthesis of Chol-TPP

Chol-TPP is a mitochondrion-targeted liposome ligand that can be used in pH and redox reactions [23]. To prepare Chol-TPP (HY-144768, MCE), which is mitochondrion-targeted and can be conjugated to liposomes, we employed a catalytic synthesis reaction based on the structure of triphenylphosphine (TPP), which condenses and connects cholesterol molecules (Chol) to the TPP structure, forming the Chol-TPP structure.

2.2. 2-DIP

2-(Diisopropylamino) ethylamine (2-DIP) is a pH-responsive chemical group that can be attached to compounds such as polyethylene glycol (PEG). PEG is a significant excipient used in the synthesis of liposomes. Prior to preparing the UA-loaded nanomaterials, we pre-prepared PEG excipients containing 2-DIP for the subsequent preparation of LNPs@UA.

2.3. Preparation of LNPs@UA

Drug-loaded liposomes (Fig. 1A) were prepared using a microfluidic mixing technique [16]. The components, namely, 1,2-dipalmitoyl-glycerol-3-phosphocholine (DPPC), grafted 2-DIP 1,2-distearoyl-glycerol-3-phosphoethanolamine- [amino (polyethylene glycol) 2000] (DSPE-PEG2000), and Chol-TPP, were dissolved in ethanol at a molar ratio of 70/5/25. The concentration of DPPC was set at 20 mmol/L to ensure complete drug encapsulation. UA and coumarin 6 (C6) were then dissolved in the lipid solutions at concentrations of 2.0 and 0.5 mg/mL, respectively. The lipid solution and PBS (0.01 mol L-1, pH = 7.4) were injected into the microfluidic mixer using a dual-channel syringe pump (LD-P2020II, Shanghai Lande Medical Equipment Co., Ltd., China) at a flow rate ratio (FRR) of 5. The lipid/UA/C6 solution was introduced through the lipid inlet, while PBS was introduced through the buffer inlet. To remove any residual organic solvents and free molecules, the resulting liposomes were dialyzed in PBS for 24 h using a dialysis bag with a molecular mass of 14000 Da.

2.4. Material characterization

The particle size, polydispersity index (PDI), and zeta potential of both the liposomal LNPs (unmodified liposomes) and LNPs@UA (TTP-modified, 2-DIP-linked, and UA-loaded liposomes) were measured using a laser particle analyser (BeNano 90 zeta, Bettersize, China) and dynamic light scattering (DLS). The blank and drug-loaded liposome samples were diluted with phosphate-buffered saline (PBS) at a ratio of 1:50. The reported values represent the average of three measurements. The morphology of LNPs@UA was observed using transmission electron microscopy (Talos™ F200X S/TEM, Thermo Fisher Scientific, USA). For TEM imaging, 20 μL of sample was dropped onto a 200-mesh copper grid. After a 30-min interval, 20 μL of a 2 % phosphotungstic acid negative staining solution was dropped onto the grid. The excess stain was subsequently removed with 30 μL of ultrapure water. Notably, the samples were allowed to air dry at room temperature for at least 5 h before being subjected to TEM.

2.5. pH response release assay

To evaluate the pH responsiveness of LNPs@UA, release experiments were conducted. A total of 10 ml of LNPs@UA was diluted in HEPES buffer solutions with pH values of 7.4 and 5.0, mimicking normal synovial fluid and OA. The diluted solutions were then placed into dialysis bags with a 50 nm pore size and placed in a 37 °C shaking incubator. At various time points (4 h, 8 h, 16 h, 28 h, and 48 h), 0.5 ml of the solution from the dialysis bags was withdrawn and analysed for UA using a multi-wavelength meter. Simultaneously, for each sample, an equal volume (0.5 ml) of fresh buffer solution was added to the dialysis bag to maintain a constant volume. The release rate of LNPs@UA at each pH value was used to assess its pH responsiveness. To ensure the precision of the results, the release analysis was performed three times, and the data were subjected to analyses.

2.6. Cell lines and cell culture

C28/I2 human chondrocytes were provided by the University of Western Australia [24]. Raw264.7 cells (mouse macrophages) were purchased from ATCC (Chinese Academy of Sciences Cell Bank, Shanghai, China) and cultured in DMEM supplemented with 10 % foetal bovine serum. To establish an in vitro inflammation model, C28/I2 cells were stimulated with 5 μg/mL LPS (HY-D1056; MCE; USA) for 12 h [17]. Similarly, a macrophage inflammation model was established by stimulating Raw264.7 cells with 1 μg/mL LPS for 12 h [18].

2.7. Western blotting analysis

After the cells were cultured, they were washed twice with PBS (P1020; Solarbio, Beijing, China). Once the residual PBS was absorbed, an appropriate volume of RIPA lysis buffer containing protease inhibitors (P0013; Beyotime; Shanghai, China) was added to the cells. The cells were then lysed on ice for 20 min. The lysate was collected in a new, sterile, enzyme-free centrifuge tube using a cell scraper. The tube was centrifuged at 4 °C and 12000 rpm for 15 min to obtain the cell protein supernatant. After BCA protein quantification, an appropriate volume of protein supernatant was added to 5 × SDS-PAGE loading buffer (P0280; Beyond; Shanghai, China). The proteins were denatured in a metal bath at 100 °C for 10 min. A total of 30 μg of protein was subsequently removed from each group for electrophoresis. After electrophoresis, the proteins were transferred to a membrane, which was blocked with 5 % skim milk powder at room temperature for 1.5 h. During this time, the sections were incubated with the primary antibody overnight. The following antibodies were used: MMP-13 (E4W3T) rabbit mAb (#69926; CST; USA), COL1A1 (E8F4L) XP® rabbit mAb (#72026; CST; USA), SQSTM1/p62 (D1Q5S) rabbit mAb (#39749; CST; USA), Beclin-1 antibody (#3738; CST; USA), LC3A/B (D3U4C) XP® rabbit mAb (#12741; CST; USA), PARK2/Parkin polyclonal antibody (14060-1-AP; Proteintech; Wuhan, China), PINK1 polyclonal antibody (23274-1-AP; Proteintech; Wuhan, China), iNOS polyclonal antibody (22226-1-AP; Proteintech; Wuhan, China), CD206 polyclonal antibody (18704-1-AP; Proteintech; Wuhan, China), GPX4 monoclonal antibody (67763-1-Ig; Proteintech; Wuhan, China), SLC7A11/xCT rabbit polyclonal (26864-1-AP; Proteintech; Wuhan, China), and ACSL4 polyclonal (22401-1-AP; Proteintech; Wuhan, China), NRF2 rabbit monoclonal (80593-1-RR; Proteintech; Wuhan, China), DHODH polyclonal antibody (14877-1-AP; Proteintech; Wuhan, China), HO-1/HMOX1 polyclonal antibody (10701-1-AP; Proteintech; Wuhan, China), P53 monoclonal antibody (60283-2-Ig; Proteintech; Wuhan, China), Bax Antibody (#2772; CST;

USA), Bcl-2 (D17C4) rabbit mAb (#3498; CST; USA), and Cleaved Caspase-3 (Asp175) antibody (#9661; CST; USA). On the second day, the membrane was washed three times for 5 min each with TBST (P1031; Solarbio, Beijing, China). After the membranes were incubated with an HRP-conjugated secondary antibody at room temperature for 1.5 h, they were washed three times for 10 min each with TBST. Lastly, the strips were exposed, and the grey value was statistically analysed using ImageJ.

2.8. RNA extraction and qRT-PCR

Total RNA was isolated and extracted from cultured cells using TRIzol reagent (Absin, Shanghai, China). A PrimeScript RT Reagent Kit (Takara, Japan) was used for reverse transcription. SYBR Green qPCR Master Mix (MCE; USA) was used for qPCR on an ABI Prism 7900HT (Applied Biosystems, CA, USA). The normalization of mRNA expression was performed using the *GAPDH* gene as a target gene with the $2^{-\Delta\Delta}$ method used to calculate the Ct value.Table 1.

2.9. ELISA assay

After the cells were cultivated under different conditions, the cell culture supernatant was collected and centrifuged at 4000 r/min for 5 min, transferred to a new sterile, enzyme-free centrifuge tube, and stored at −80 °C for future use. Then, the expression of TNF-α, IL-6 and IL-1β was detected in accordance with the operating instructions of the corresponding commercial reagent kits. Human TNF-α ELISA kits (Item No. SEKH-0047; Manufacturer: Solarbio Life Sciences); Human IL-6 ELISA kits (Item No. SEKH-0013; Manufacturer: Solarbio Life Sciences); Human IL-1β ELISA kits (Item No. SEKH-0002; Manufacturer: Solarbio Life Sciences) were used.

2.10. Mitochondria-targeting ability

C28/I2 cells were inoculated into a confocal dish at a suitable density and grown until the second day. Then, LNPs@UA-C6 and LNPs@C6 were added to the cells for more than 12 h and the original medium was discarded. Precooled PBS was added to wash the cells three times, and the medium was prepared as a mixture with a mitochondrial far-infrared fluorescent probe (Mito-Tracker Deep Red FM; Beyotime; Shanghai, China) at a ratio of 5000:1. The mixture was subsequently added to the cultured C28/I2 cells, which were then incubated for 30 min. After that, the medium was discarded, and the cells were washed with precooled PBS three times before they were photographed with PBS under a laser confocal microscope.

Table 1
The primers are listed in Table 1.

Gene	Forward 5′-3′	Reverse 5′-3′
TNF-α	TGTTCCTCAGCCTCTTCT	GGACCTGGGAGTAGATGA
IL-6	AAGTCCTGATCCAGTTCCT	GCAGAATGAGATGAGTTGTC
IL-1β	ATCTCCGACCACCACTAC	CACCACTTGTTGCTCCAT
NRF2	ATTCCTTCAGCAGCATCC	GTGTTGACTGTGGCATCT
ASCL4	TGCGTGAACGAGGGCTAT	GCAGGTGCTTGATGTAGTC
SLC7A11	TTCAAGGTGCCACTGTTC	TGATGACGAAGCCAATCC
DHODH	GGAAGAACAAGACCTCAGT	GGACACATTCACCACCAG
GPX4	GCTGTGGAAGTGGATGAA	GATGAGGAACTGTGGAGAG
HO-1	TGACACCAAGGACCAGAG	AAGGACCCATCGGAGAAG
GAPDH	TATGACAACAGCCTCAAGAT	AGTCCTTCCACGATACCA
Tnf-α	GTGGAACTGGCAGAAGAG	GCTACAGGCTTGTCACTC
Il-1β	CTTCAGGCAGGCAGTATC	CAGCAGGTTATCATCATCATC
Il-6	TTCCATCCAGTTGCCTTC	AATTAAGCCTCCGACTTGT
Inos	CAGGAGATGTTGAACTATGTC	TTGGTGTTGAAGGCGTAG
Cox-2	CCTTCTCCAACCTCTCCTA	CTCCACCAATGACCTGATAT
Gapdh	TCTCCTGCGACTTCAACA	TGTAGCCGTATTCATTGTCA

2.11. Cellular viability

After the C28/I2 cells were cultured for 24 h, different concentrations of LNPs@UA and LPS were added and processed, and then 10 μL of CCK-8 operating solution was added for 2 h of cultivation. The OD value was detected at a wavelength of 450 nm by an enzyme marker to calculate the corresponding proliferative activity level.

2.12. Cell apoptosis analysis

Following the different cultivation treatments, the corresponding reaction reagents were added to the cells in each group according to the instructions for the kits. C28/I2 cells were incubated with annexin V-FITC/PI for 15–30 min, after which the apoptosis rate of each group of cells was analysed with an apoptosis detection kit (Becton Dickinson Biosciences, San Jose, CA, USA).

2.13. ROS assay

After the different cultivation treatments, the corresponding reaction reagents were added to each group of cells as required by the instructions of the reagent kit. The ROS levels of the cells were analysed with a flow cytometer (Becton Dickinson Biosciences). The Reactive Oxygen Species Detection Kit (Beyotime; item number: S0033S) was purchased from Beyotime.

2.14. Detection of the Fe^{2+} content

After the different cultivation treatments, the corresponding lysate was added to each group of cells according to the instructions for the reagent kit. After that, the OD values of each group of samples were detected by ELISA (Solebao, BC5310).

2.15. SOD, GSH and ATP assay

After the different cultivation treatments, the corresponding extracting solution was added to each group of cells according to the instructions for the kits. The reaction reagents were subsequently added to the cells whose OD values were detected by ELISA (Beyotime, S0101S; Beyotime, S0053; Beyotime, S0026).

2.16. RNA sequencing and bioinformatic analysis

Following the cultivation treatments, the C28/I2 cells were washed twice with precooled PBS and treated with an appropriate amount of the RNA extraction reagent TRIzol (Absin, Shanghai, China). The total RNA was extracted according to the experimental procedures specified by the gene-sequencing company to establish an RNA library for subsequent transcriptome sequencing. The sequenced data were analysed using bioinformatic techniques such as differential gene expression analysis, in GO/KEGG, and GSEA.

2.17. ACLT-induced OA mouse model

The University of South China Ethics Committee for Animal Experiments authorized all the animal handling reported here as being morally appropriate and ensured that it complied with any regulations (Approved number: 2023-253). The OA mouse model was constructed by ACLT. The mice were anaesthetized with isoflurane gas and placed in a supine position after the surgical area was prepared for skinning. Each right knee joint, which served as the surgical site, was thoroughly disinfected. A microblade was used to incise the skin, exposing the patellar ligament. The joint cavity was then opened along the medial edge of the patellar ligament, and the adipose tissue surrounding the joint cavity was gently separated. The tibial end of the anterior cruciate ligament is located along the anterior medial edge of the tibia and is subsequently

cut off to induce instability in the knee joint. The wound was cleaned using iodophor antiseptic solution, and the tissue and skin were closed using continuous 7–0 surgical sutures. To prevent wound infection, penicillin was locally injected. Fifty 8-week-old male C57BL/6 mice were obtained from Vital River Laboratory Animal Technology Co. Ltd. (Beijing, China). The mice were randomly divided into 5 groups, with each group consisting of 10 mice. Group 1 served as the negative control group and underwent sham surgery in which only the joint capsule was dissected, and the skin was sutured layer by layer. These mice were injected with saline. The mice in groups 2–5 underwent ACLT surgery for OA modelling. In group 2, all the mice were injected with saline after 3 days of ACLT construction to establish the OA model. In contrast, the mice in groups 3–5 received injections of 10 μL of different drugs (namely, LNPs, UA, or LNPs@UA) into the joint cavity every 3 days for a period of 6 weeks after 3 days of ACLT construction. The mice were housed in a controlled environment with SPF-grade standards, in which a temperature of approximately 25 °C was maintained. They were also provided with an adequate supply of food, water, and new wood shavings every 3 days.

2.18. Histological and immunohistochemical analyses

Six weeks after the surgery, the knee joints of the mice were isolated after the animals were euthanized. These isolated joints were fixed with paraformaldehyde and cut into 5 μm-thick slices after they were decalcified and embedded in paraffin. The slices were stained with H&E and Safranin O-Fast Green for histological analysis. For immunohistochemical staining, the slices were incubated with the corresponding primary antibodies (e.g., against MMP13, Col-II, IL-1β, PINK1, Parkin, p62, Beclin1, ASCL4 and GPX4) overnight at 4 °C, followed by incubation with secondary antibodies for 1 h. The paraffin slices were stained with 3,3′-diaminobenzidine (DAB) substrate. Lastly, the relative expression of these genes was quantified using ImageJ software.

2.19. Statistical analysis

The data are presented as the means of at least three biological replicates with standard deviations. For normally distributed data, the differences between the two groups were assessed by bilateral *t*-test. $p < 0.05$ was considered significant. All the statistical analyses were conducted using GraphPad Prism 9.

3. Results

3.1. Synthesis and characterization of LNPs@UA

Both LNPs and LNPs@UA were synthesized and prepared using microfluidic technique, as shown in Fig. 1A. To study the physicochemical properties of LNPs@UA, transmission electron microscopy (TEM) and dynamic light scattering (DLS) were employed, and the results revealed that the LNPs and LNPs@UA were uniformly complete spheroids measuring ≈ 127.3 ± 1.35 and 125.6 ± 12.51 nm, respectively (Fig. 1B and C). Moreover, the polydispersity indices (PDIs) of the LNPs and LNPs@UA were approximately 0.2136 ± 0.02223 and 0.1723 ± 0.03995, respectively (Fig. 1B). As shown in Fig. 1D, the zeta potential values for LNPs and LNPs@UA were approximately −16.9033 ± 0.7877 mV and −11.2166 ± 2.378 mV, respectively. The release behavior of UA wrapped in LNP@UA in solutions with different pH values was subsequently detected. The results revealed that approximately 48.2 % of the UA was released when LNP@UA was added to an environment at pH 5.0 at 28 h, however, when the environment at pH 7.4, only 15.2 % of the UA was released within the same time frame (Fig. 1E). Notably, the release rate of pure UA solution showed no significant change at pH 5.0 and pH 7.4, reaching approximately 80 % after 16 h with no further notable increase thereafter (Fig. 1E). The TEM images further confirmed that, following 24 h of treatment in a pH 5.0 solution, LNPs@UA experienced substantial dissociation. As shown in Fig. 1F, the previously homogeneous spherical structure of LNPs@UA transitioned into an irregular morphology. Collectively, these results indicate that LNPs and LNPs@UA have uniform particle sizes, relatively low potential energies, good stabilities, and equally distributed molecular weights.

3.2. Biocompatibility and mitochondrion-targeted behaviors of LNPs@UA

To investigate the effect of LNPs@UA on cell viability, a CCK8 assay was performed after the administration of LNPs@UA for 24 h in C28/I2 chondrocytes and RAW264.7 macrophages. As shown in Fig. 2A, LNPs@UA had no significant toxic effect on C28/I2 chondrocytes at different concentrations (1, 5, 10, 20, 50, 100 and 250 μM). Interestingly, at a concentration of 20 μM, LNPs@UA somewhat enhanced the activity of C28/I2 cells. Similar results were observed in RAW264.7 cells, and LNP@UA significantly increased the activity of RAW264.7 cells at a concentration of 20 μM (Fig. 2B). These results suggest the satisfactory biocompatibility of LNPs@UA at a dose of 20 μM or less in C28/I2 chondrocytes or RAW264.7 macrophages, which could be used for follow-up studies without compromising cell activity.

After determining the safe concentration range, we sought to test whether LNPs@UA could efficiently target mitochondria. The fluorescent dye coumarin 6 (C6) was loaded onto LNPs@UA and LNPs, and MitoTracker was used to track the intracellular transportation of LNPs@UA and LNPs. A confocal laser scanning microscope (CLSM) was then used to observe the result. As shown in Fig. 2C, compared with the LNPs, LNPs@UA displayed highly efficient accumulation in the mitochondrial structure, which was also confirmed by qualitative colocalization analysis (Fig. 2D), suggesting that LNPs@UA exhibited exceptional mitochondrial targeting in chondrocytes.

3.3. Anti-inflammatory effects of LNP@UA

Previous studies have shown that UA has extremely potent anti-inflammatory effects [6]. Based on the anti-inflammatory effect of UA, we conducted experiments on C28/I2 chondrocytes and RAW264.7 macrophages to analyse the in vitro anti-inflammatory effects of LNPs@UA. C28/I2 cells were stimulated with 5 μg/ml LPS for 12 h to establish a cellular inflammation model, after which 20 μM LNPs@UA or 20 μM UA was added. As shown in Fig. 3A–C, the RT-qPCR results revealed that the mRNA levels of proinflammatory genes, including *TNF-α, IL-1β* and *IL-6*, were increased when the cells were stimulated with LPS but significantly decreased after treatment with LNPs@UA. Consistent with the RT-qPCR results, the ELISA results revealed that the levels of TNF-α, IL-6, and IL-1β significantly increased by approximately 4-fold in C28/I2 cells induced by LPS. However, the expression of TNF-α, IL-6, and IL-1β decreased by approximately half after treatment with LNPs@UA and UA, with LNPs@UA resulting in a more pronounced reduction than UA did (Supporting Information Figure S1). Moreover, the Western blotting results indicated that LNPs@UA promoted the expression of COL-II while suppressing MMP-13 protein expression (Fig. 3D–F). M1 macrophages can secrete inflammatory cytokines such as TNF-α, IL-6, and IL-1β, which act on C28/I2 chondrocytes and lead to cell destruction, while M2 macrophages can protect against it (Fig. 3G). To verify the anti-inflammatory effect of LNPs@UA, we applied 1 μg/ml LPS to stimulate RAW264.7 mouse macrophages for 12 h before establishing an inflammatory model. LNPs@UA or UA was added to the cultures, and the cells were treated. Previous studies revealed that the repolarization of M1 macrophages into M2 macrophages has been shown to block the development of OA successfully [25]. The RT-qPCR results revealed that, compared with the control group, LPS significantly increased the expression of the inflammatory factors *Tnf-α, Il6, Il1β, Cox2*, and *Inos* (increased of approximately four-fold), and decreased the expression of *Cd206*, which is a marker gene of M2 macrophages. However, LNPs@UA effectively suppressed the expression levels of

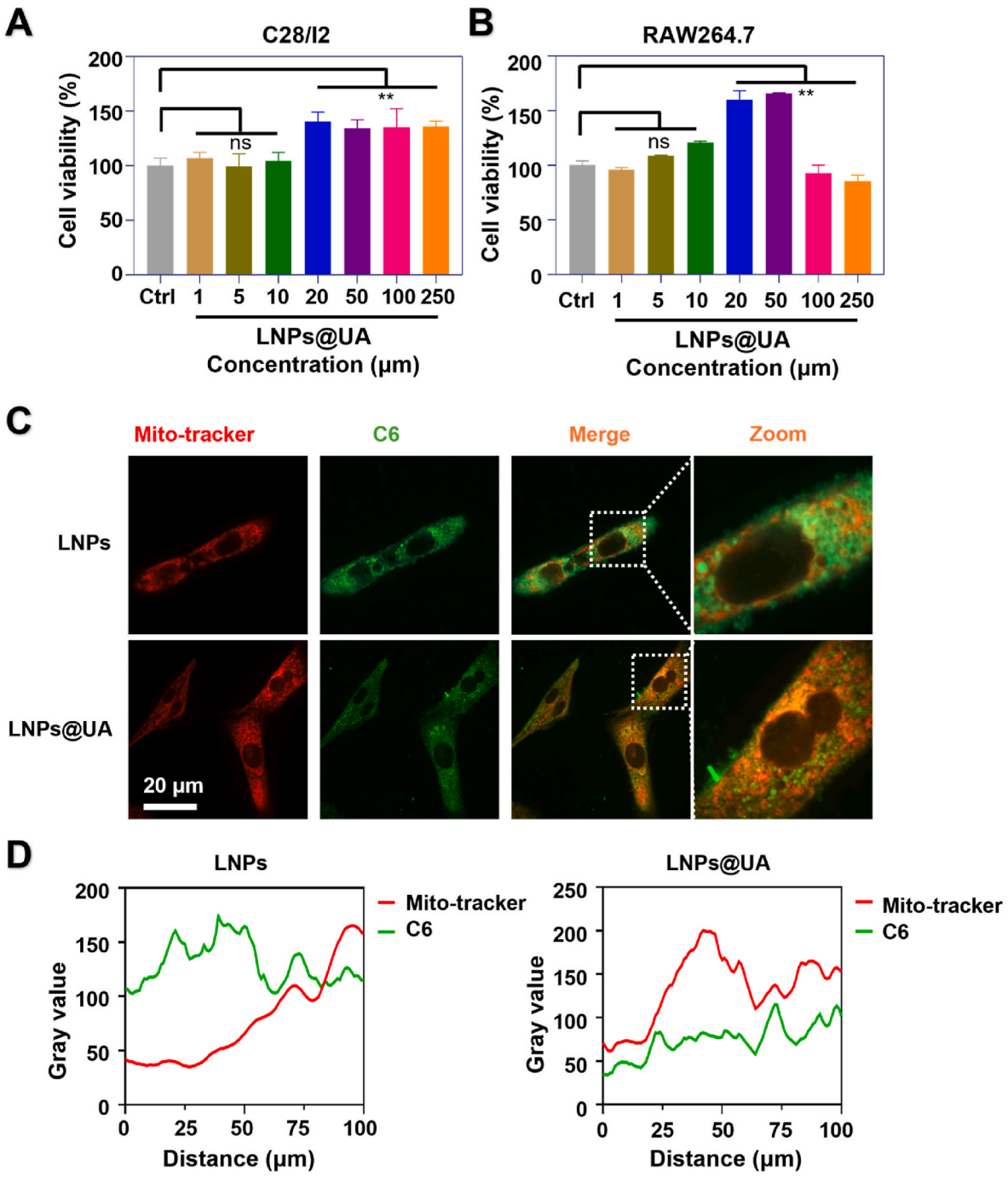

Fig. 2. Biocompatibility and mitochondrion-targeted behaviors of LNPs@UA. (A–B) The viability of C28/I2 (n = 5) and RAW264.7 (n = 3) cells treated with different concentrations of LNPs@UA was detected by CCK-8 assay. (C) Mitochondrial targeting ability of LNPs and LNPs@UA (green: C6; red: MitoTracker). (D) Qualitative analysis of mitochondrial colocalization by imaging software. ns indicates no significance, $^{**}p < 0.01$, ns indicates not significance.

these genes, and elevated the expression levels of *Cd206* in RAW264.7 mouse macrophages, resulting in a more significant anti-inflammatory effect than UA did (Fig. 3H–I and Supporting Information Figure S2). The protein level of RAW264.7 mouse macrophages was detected by Western blotting to evaluate the effect of LNPs@UA on its repolarization. As shown in Figure J–L, LNPs@UA significantly inhibited the protein expression of the LPS-induced M1 macrophage-polarizing molecule iNOS and increased the protein expression of the M2 macrophage-polarizing molecule CD206, suggesting that LNPs@UA significantly inhibited M1 macrophage polarization and promoted M2 macrophage repolarization.

3.4. In vitro scavenging of ROS and the mitophagy-enhancing effect of LNPs@UA

To confirm the protective effect of LNPs@UA on chondrocytes in vitro, we assessed the antioxidative effects of LNPs@UA on LPS-treated C28/I2 cells by flow cytometry (FCM). The results demonstrated that the ROS level significantly decreased with UA and LNP@UA treatment in C28/I2 chondrocytes stimulated with LPS (Fig. 4A). Moreover, FCM was used for quantitative analysis. As shown in Fig. 4B, the percentage of DCFH-DA-positive cells was 60.6 % in the LPS-treated group but was reduced to 43.3 % and 23.0 % in the UA- and LNP@UA-treated groups, respectively.

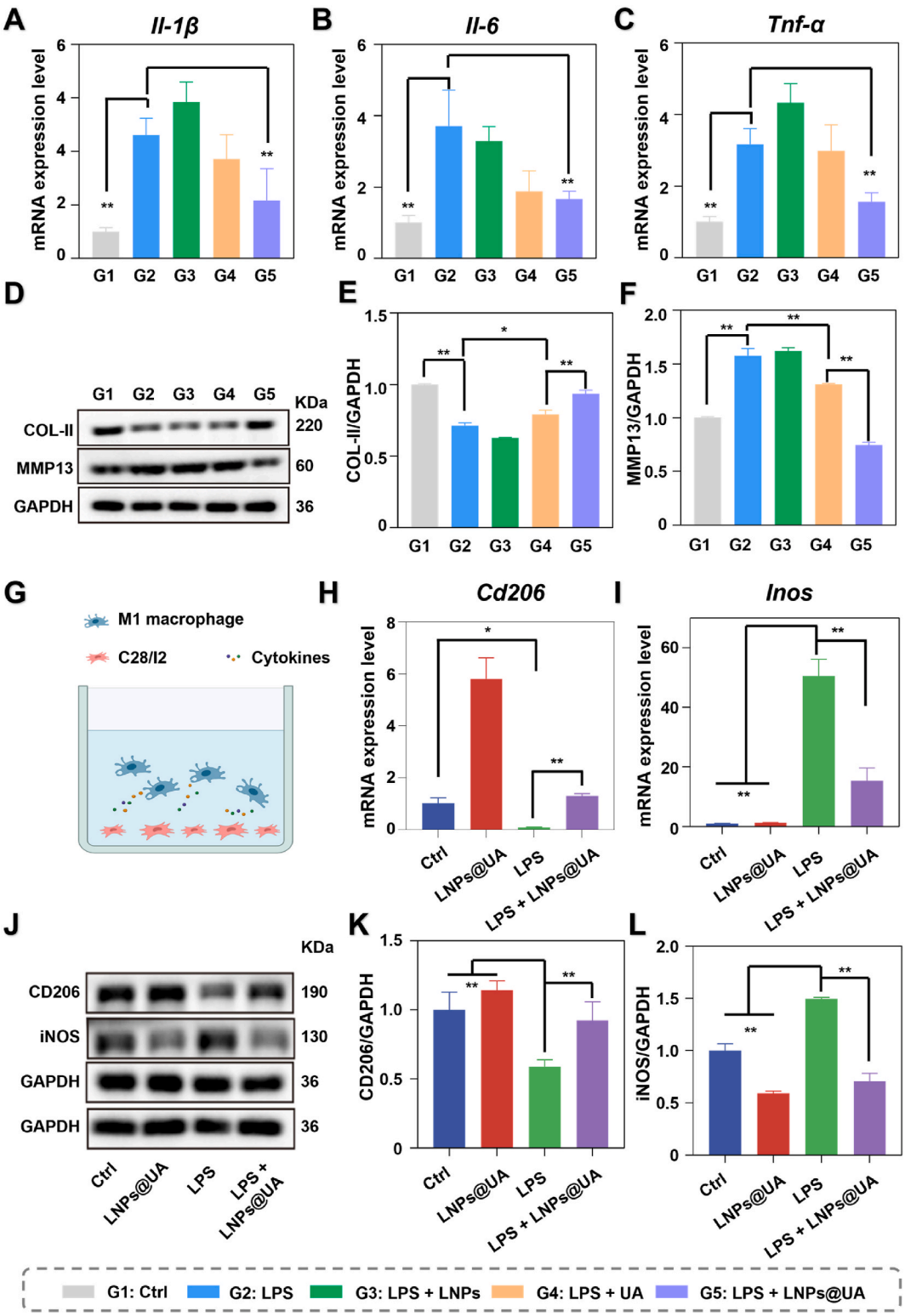

Fig. 3. Anti-inflammatory effects of LNPs@UA. (A–C) The mRNA expression of *Il-1β*, *Il-6* and *Tnf-α* was measured by qRT-PCR in C28/I2 cells treated with different drugs (n = 4). (D–F) Western blotting showing the expression of COL-II and MMP-13 in C28/I2 cells treated with different drugs (n = 3). (G) Schematic diagram showing that RAW264.7 cells act on C28/I2 cells by secreting cytokines. (H–I) The mRNA expression of *Cd206* and *Inos* in RAW264.7 cells in different groups were detected by RT-PCR (n = 4). (J–L) Western blotting was used to measure the expression of CD206 and iNOS in RAW264.7 cells treated with different drugs, which were then quantified (n = 3). $^{*}p < 0.05$, $^{**}p < 0.01$.

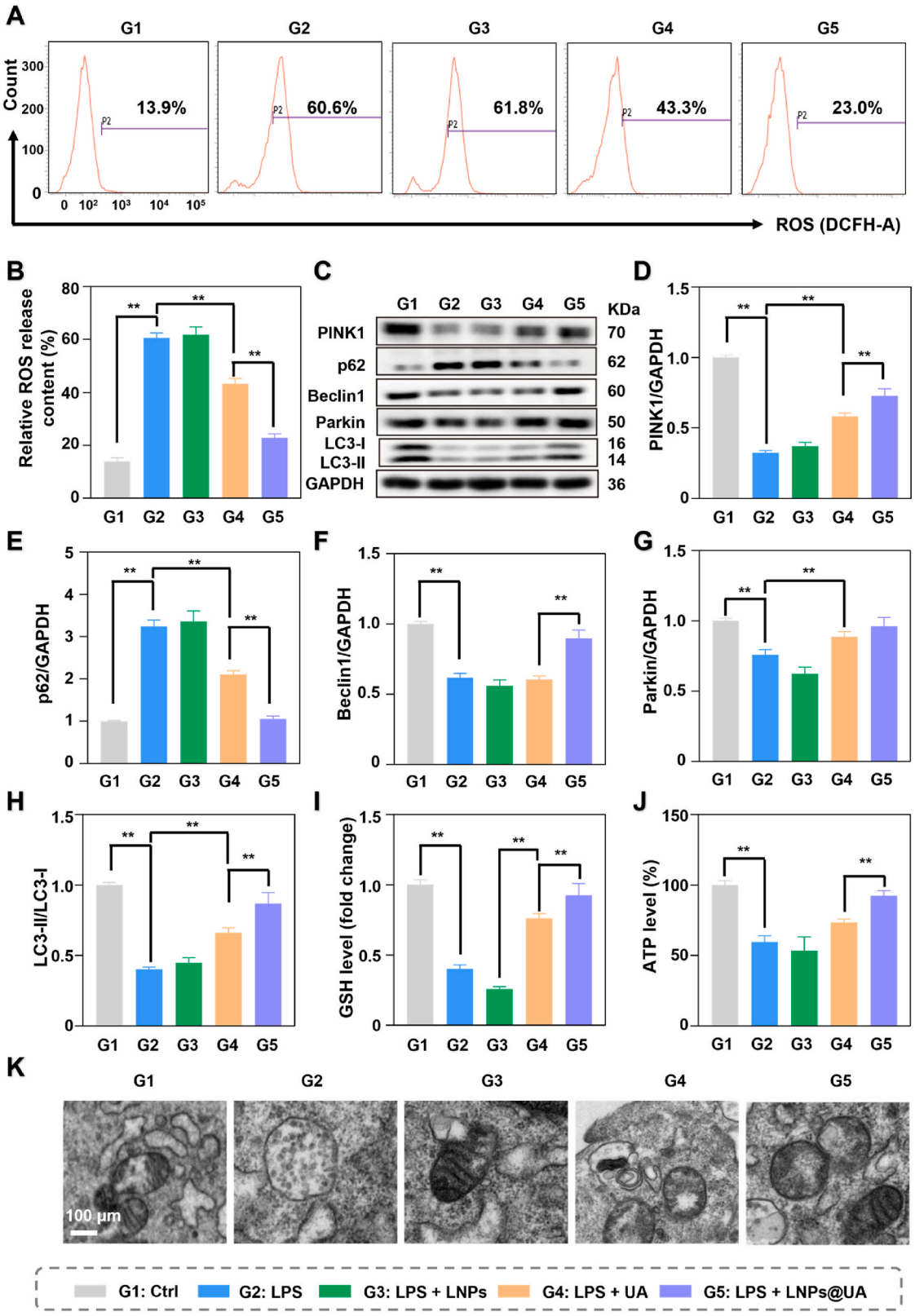

Fig. 4. In vitro scavenging of ROS and mitophagy-enhancing effects of LNP@UA. (A–B) ROS levels in C28/I2 cells treated with different drugs were measured and quantified using FCM (n = 3). (C) Western blot analysis of the expression of PINK1, p62, Parkin, Beclin1 and LC3-II/LC-I in C28/I2 cells treated with different drugs. (D–H) Quantification of PINK1, p62, Parkin, Beclin1 and LC3-II/LC-I (n = 3). (I) GSH levels in C28/I2 cells in different groups were detected (n = 5). (J) ATP levels in C28/I2 cells in different groups were detected (n = 5). (K) Mitochondrial morphology of C28/I2 cells treated with different drugs was observed via bio-TEM. $^{**}p < 0.01$.

During mitophagy, the serine/threonine kinase PINK1 works with PRKN/parkin to label damaged mitochondria for degradation in lysosomes [26]. Moreover, Beclin1 and LC3-II orchestrate the formation of autophagosomes, which envelop damaged mitochondria, while SQSTM1/p62 serves as a bridge, linking ubiquitinated cargo to the autophagosomal membrane [27]. Based on the excellent ROS scavenging effects of LNPs@UA, mitochondria might be identified as the key organelles involved in this action. To investigate the effects of LNPs@UA on mitophagy and mitochondrial structure, we first examined the changes in mitophagy markers by Western blotting. LPS exposure significantly reduced mitophagy in C28/I2 cells, as shown by the decreased expression levels of PINK1, Parkin, Beclin1 and LC3-II and increased expression levels of SQSTM1/p62, whereas LNPs@UA and UA increased the expression levels of PINK1, Parkin, Beclin1, and LC3-II and decreased the expression of SQSTM1/p62 (Fig. 4C–H). Additionally, the level of intracellular GSH can be used to measure an organism's ability to resist oxidative stress [28]. A GSH assay kit was used to determine the amount of GSH present in the C28/I2 cells. As shown in Fig. 4I, UA and LNPs@UA considerably improved the intracellular GSH level, providing further evidence of the ability of LNPs@UA to suppress the responsiveness of chondrocytes to oxidative stress. Moreover, the regulatory effect of LNPs@UA on energy metabolism was assessed in chondrocytes using the adenosine triphosphatase (ATP) assay. As shown in Fig. 4J, LNPs@UA greatly increased intracellular ATP synthesis, suggesting that it could restore mitochondrial function in chondrocytes. The structure of the mitochondria was further studied by biological TEM. As shown in Fig. 4K, LNPs@UA significantly restored the mitochondrial structure and cristae in the LPS-induced chondrocytes. Consequently, LNPs@UA could suppress the level of ROS by enhancing mitophagy in C28/I2 chondrocytes, thereby strengthening mitochondrial function.

3.5. *In vitro inhibition of the ferroptosis effects of LNPs@UA*

Excess mitochondrial damage-induced ROS release may lead to protein lipid peroxidation and subsequent ferroptosis, which we hypothesized could be mitigated by LNPs@UA. GPX4 is an important

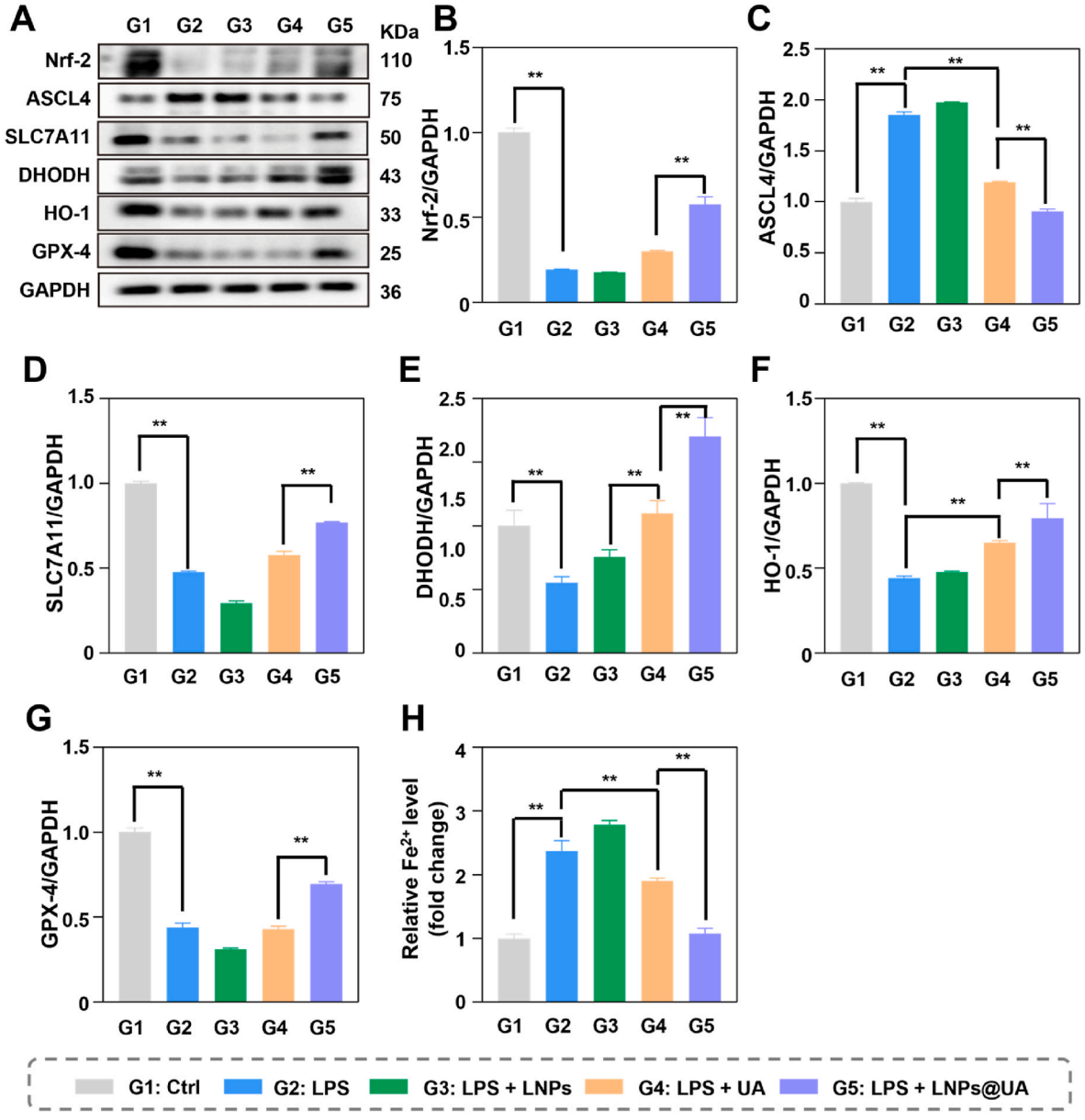

Fig. 5. In vitro inhibited ferroptosis effects of LNPs@UA. (A–G) Western blot analysis of Nrf-2, ASCL4, SLC7A11, DHODH, HO-1 and GPX4 in each group (n = 3). (H) The Fe^{2+} contents of each group were detected (n = 5). $^{**}p < 0.01$.

marker of ferroptosis, and its downregulation can increase the sensitivity of chondrocytes to oxidative stress and aggravate ECM degradation [29]. In addition, icariin can attenuate chondrocyte ferroptosis and articular cartilage damage by enhancing the SLC7A11/GPX4 axis in OA [30]. A recent study revealed that quercetin could modulate ferroptosis through the SIRT1/Nrf-2/HO-1 pathway and alleviate cartilage destruction in OA [31]. To obtain further insights into how LNPs@UA inhibited the intracellular inflammatory response, the molecular

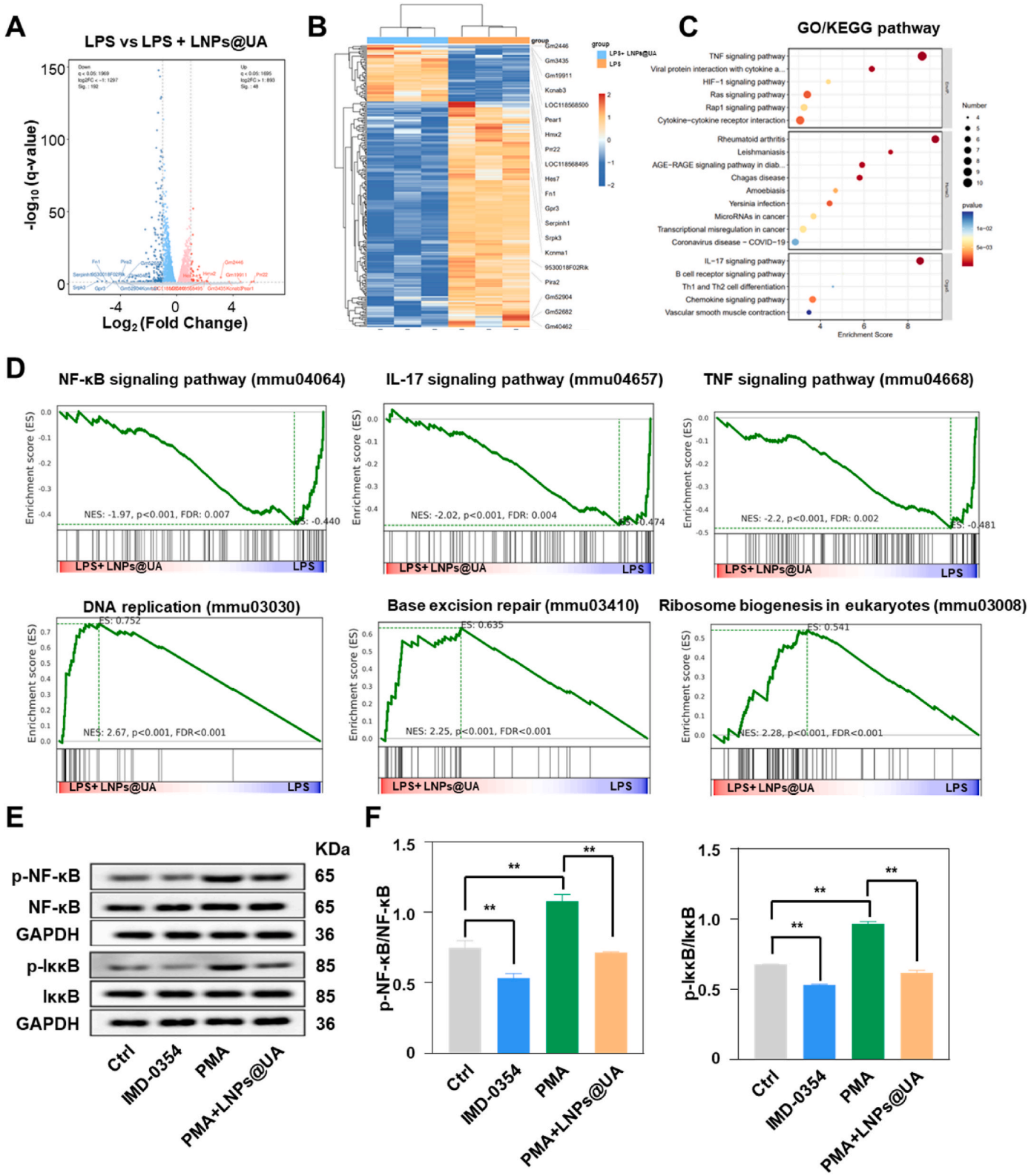

Fig. 6. Transcriptomic sequencing analysis of LNPs@UA. (A) Volcano plot showing that the gene expression of C28/I2 cells was regulated by LNP@UA treatment. (B) Heat map analysis of DEGs between the LPS group and the LPS + LNPs@UA group. (C) GO and KEGG enrichment analyses of differentially expressed genes. (D) GSEA results between the LPS group and the LPS + LNPs@UA group. (E–F) Western blotting analysis of p-NF-κB and NF-κB and p-IκκB and IκκB. $^{**}p < 0.01$, n = 3.

mechanism of ferroptosis was investigated by Western blotting. The results demonstrated that the expression of ACSL4 increased with LPS stimulation but was greatly reduced in the LNP@UA treatment groups. Moreover, LNPs@UA greatly increased the expression of SLC7A11, GPX4, HO-1, DHODH, and Nrf-2 in C28/I2 cells stimulated with LPS (Fig. 5A–G). In particular, compared with that in the control group, the expression level of GPX4 was reduced by 56.1 % in the LPS treatment group, but the expression level of LNPs@UA increased by 25.7 % in the LPS treatment groups. Moreover, in LPS-treated C28/I2 cells, LNPs@UA and UA were evaluated for their ability to modulate the release and content of ferrous ions (Fe^{2+}), with assays showing that LNPs@UA and UA effectively decreased LPS-augmented Fe^{2+} levels (Fig. 5H). Overall, LNPs@UA inhibited the ferroptosis of C28/I2 chondrocytes induced by LPS, thereby enhancing their mitophagy function and suppressing the inflammatory response.

3.6. Transcriptomic sequencing analysis of LNPs@UA and validation of the NF-κB signaling pathway

To gain further insight into the anti-inflammatory mechanism of LNPs@UA, RNA sequencing was performed on LPS-activated chondrocytes treated with LNPs@UA. As shown in Fig. 6A, the volcano plots revealed that 1695 genes were significantly upregulated, whereas 1969 genes were downregulated after LNPs@UA treatment. The heat map shows that LNPs@UA treatment had a similar suppressive effect on the expression of various proinflammatory genes (Fig. 6B). To investigate the effects of LNP@UA treatment on potential signaling pathways, KEGG and GO enrichment analyses were conducted to identify the top 20 enriched pathways (with the smallest Q values). The TNF signaling pathway and the IL-17 signaling pathway are closely related to the anti-inflammatory effects of LNPs@UA (Fig. 6C). Moreover, gene set enrichment analysis (GSEA) confirmed that the NF-κB signaling pathway, the IL-17 signaling pathway and the TNF signaling pathway were significantly suppressed after LNP@UA treatment and that DNA replication, base excision repair and ribosome biogenesis in eukaryotes were markedly increased after LNP@UA treatment (Fig. 6D).

To validate the effects of LNPs@UA on the NF-κB signaling pathway, we performed Western blotting with the NF-κB inhibitor IMD-0354 (IKK2 inhibitor V) and the agonist phorbol 12-myristate 13-acetate (PMA) to analyse the NF-κB signaling pathway. As shown in Fig. 6E, compared with those in the PMA treatment group, the expression of p-NF-κB and p-Iκκβ significantly decreased after LNP@UA treatment, which was almost the same as that in the control group, suggesting that LNPs@UA and IMD-0354 have similar functions, both of which significantly inhibit the activation of the NF-κB signaling pathway (Fig. 6E and F).

3.7. LNPs@UA protect against articular cartilage injury and enhance anti-inflammatory effects in OA mice

Based on the excellent anti-inflammatory effects of LNPs@UA in vitro, we further explored their therapeutic potential in ameliorating OA using an anterior cruciate ligament transection (ACLT)-induced OA mouse model. As previously reported, the pathology of OA typically involves progressive cartilage defects, the loss of extracellular matrix (ECM) and subchondral bone remodeling [32]. The knee joint sections were stained with hematoxylin–eosin (H&E) to assess cartilage surface injury. As shown in Fig. 7A, the saline group maintained a smooth cartilage surface, orderly chondrocyte arrangement and unaltered joint space, whereas severe cartilage erosion and disordered chondrocytes were observed in the ACLT-induced OA group. In comparison, in LNP@UA-treated ACLT mice, the erosion and degeneration of the cartilage layer were significantly reduced. Furthermore, the safranin O-fast green (S&F) staining results were consistent with the results of the H&E staining, which revealed increased proteoglycan content and even matrix distribution in ACLT-induced OA mice after LNPs@UA treatment (Fig. 7B). Moreover, immunohistochemistry (IHC) analysis demonstrated that LNPs@UA significantly attenuated matrix metalloproteinase (MMP)-13 expression and enhanced collagen type II (COL-II) expression, indicating an important role for LNPs@UA in curtailing articular matrix degradation (Fig. 7C–D, F-G). Overall, LNPs@UA significantly protected against articular cartilage injury and ECM loss in ACLT-induced OA mice.

In addition, to validate the anti-inflammatory effect of LNPs@UA in vivo, the IHC staining of proinflammatory cytokines such as IL-1β was performed in knee synovial tissues. Compared with those in the ACLT-induced OA group, the IL-1β levels in synovial tissues were significantly lower after treatment with LNPs@UA, indicating that LNPs@UA effectively reduced the levels of proinflammatory factors in the synovium and thus alleviated synovitis and articular cartilage injury in OA patients (Fig. S3, Supporting Information). Moreover, to study the effect of LNPs@UA on the polarization of synovial macrophages in ACLT-induced OA mice, the relative fluorescence intensities of iNOS and CD206 in synovial tissues were determined by immunofluorescence (IF) staining. The results revealed that the relative fluorescence intensity of iNOS in the ACLT-induced OA group was significantly greater than that in the saline group, whereas the relative fluorescence intensity of CD206 was not significantly different. In contrast, following treatment with UA or LNPs@UA, the relative fluorescence intensity of iNOS was significantly reduced, whereas that of CD206 was significantly increased (Fig. 7E–H-I). These results collectively indicate that LNPs@UA can reduce the population of M1 macrophages and increase the polarization of M2 macrophages, thereby suppressing synovial inflammation in OA model mice.

To verify the biosafety of LNPs@UA, we explored the main organs of the mice by histopathological analysis. The results revealed no significant changes in the H&E-stained heart, liver, spleen, lungs or kidneys after treatment with LNPs, UA or LNPs@UA (Fig. S4, Supporting Information). Consequently, LNP@UA is a highly safe treatment for OA.

3.8. In vivo LNP@UA inhibits ferroptosis by enhancing mitophagy

The in vitro results demonstrated that LNPs@UA could increase the level of mitophagy in C28/I2 chondrocytes, but the effect of LNPs@UA in vivo is unclear. To this end, we tested the mitophagy markers Beclin-1 and p62 by using IHC staining. Compared with those in the ACLT-induced OA group, the number of Beclin-1-positive cells significantly increased after LNP@UA treatment. Moreover, the number of p62-positive cells was significantly decreased in ACLT-induced OA mice after LNP@UA treatment (Fig. 8A–B, F-G). These results are consistent with the results of the in vitro experiments, suggesting that LNPs@UA can significantly increase the level of mitochondrial autophagy in OA mice.

To verify the ferroptosis-inhibiting effects of LNPs@UA, we tested the expression of the ferroptosis markers GPX4, ASCL4 and SLC7A11 using IHC staining. Compared with those in the ACLT-induced OA group, the number of GPX4-and SLC7A11-positive cells in the articular cartilage of OA patients significantly increased after LNP@UA treatment, and the number of ASCL4-positive cells significantly decreased, indicating that LNP@UA significantly inhibited ferroptosis in the articular cartilage of OA mice (Fig. 8C–E, H-J). In summary, these results suggest that LNPs@UA significantly improve ferroptosis in OA and that the ability of LNPs@UA to inhibit ferroptosis is greater than that of UA.

4. Discussion

Chronic inflammation of synovial tissue is a hallmark feature of OA, contributing significantly to disease progression and articular cartilage degeneration. Numerous researchers have attempted to attenuate OA progression by targeting chronic synovial inflammation, yet the outcomes have been largely unsatisfactory. Challenges in previous research include difficulties in specific synovial tissue targeting and

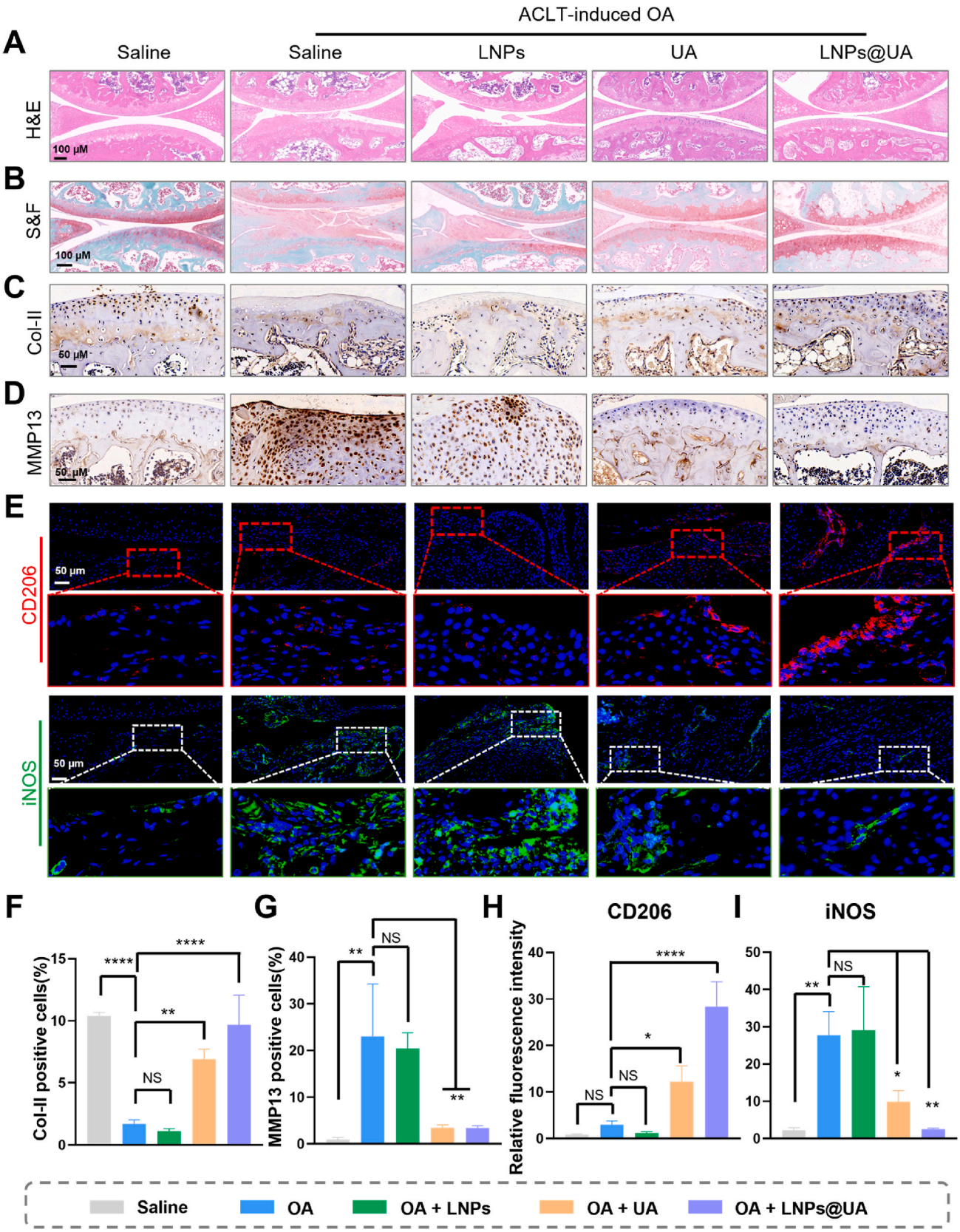

Fig. 7. LNP@UA improved articular cartilage injury and enhanced anti-inflammatory effects in OA model mice. (A) Medial compartment cartilage and subchondral bone of knee joints were stained with H&E and (B) S&F. (C–D) Col-II and MMP-13 immunohistochemistry of knee joint medial compartment cartilage. (E) CD206 and iNOS immunofluorescence in knee joint synovial tissue. Quantitative analysis of (F) Col-II, (G) MMP-13, (H) CD206 and (I) iNOS expression. NS indicates no significance, $^{*}p < 0.05$, $^{**}p < 0.01$, and $^{****}p < 0.0001$, n = 3.

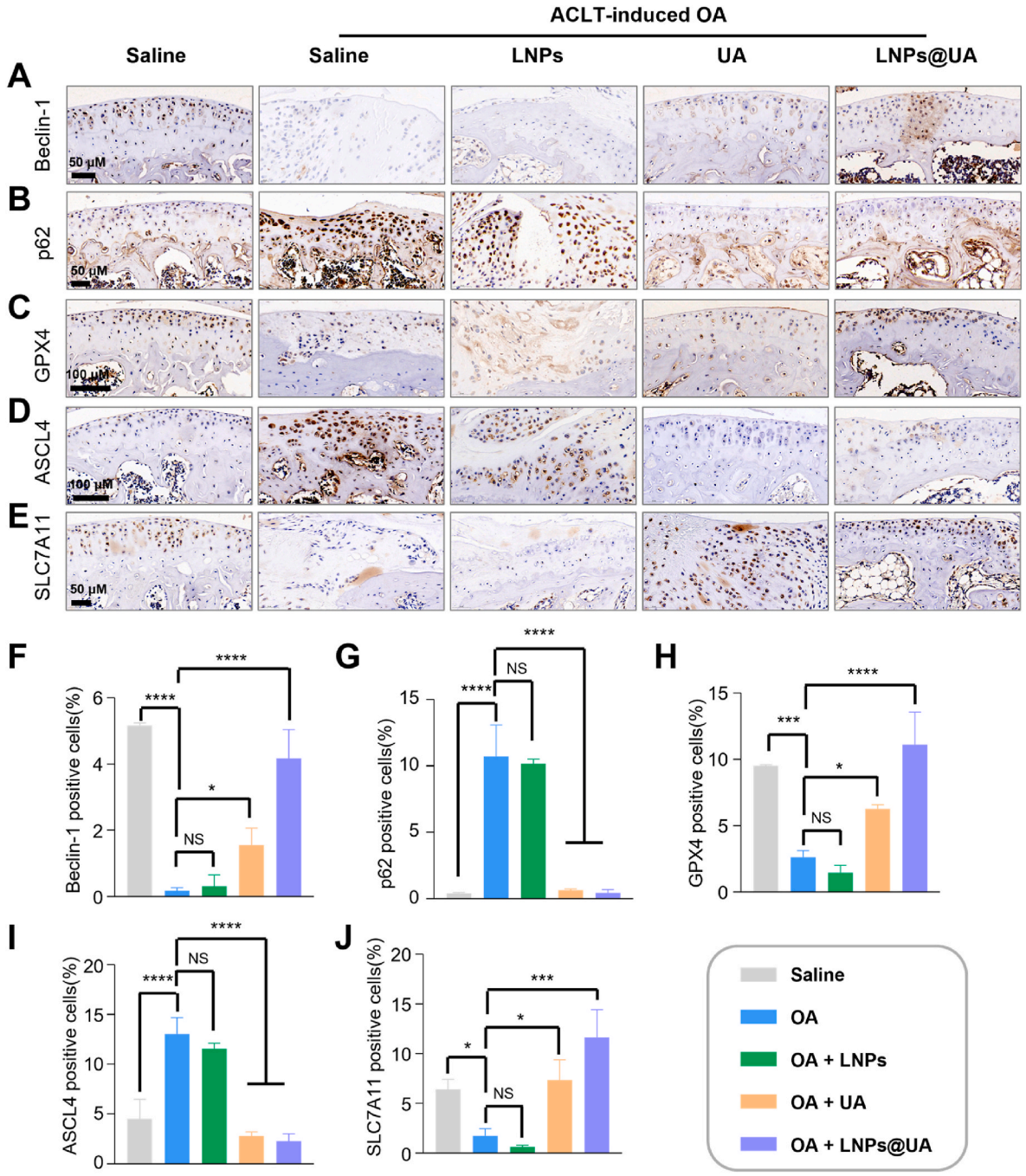

Fig. 8. In vivo, LNPs@UA inhibited ferroptosis by enhancing mitophagy. (A–E) Beclin-1, p62, GPX4, ASCL4 and SLC7A11 immunohistochemistry of knee joint medial compartment cartilage. (F–I) Quantitative analysis of Beclin-1, p62, GPX4, ASCL4 and SLC7A11 expression. NS indicates no significance, $^{*}p < 0.05$, $^{***}p < 0.001$, and $^{****}p < 0.0001$, n = 3.

individualized variations in joint cavity microenvironments influenced by synovitis, hindering the achievement of consistent therapeutic outcomes within a single treatment modality. Drawing on the mildly acidic microenvironment present in osteoarthritic joint cavities and the role of mitochondria-derived ROS in initiating chronic joint inflammation, we developed nanoparticles using microfluidic technology. Although the field of pH-responsive nanomaterials has been well explored, these nanomaterials have some limitations, such as poor targeting ability. In this study, we developed a pH-responsive and mitochondrion-targeting nanocarrier system with improved targeting ability and enhanced bioavailability. These nanoparticles encapsulate anti-inflammatory agents such as UA within LNPs, which are modified with 2-DIP and TPP. The former enables pH-responsive drug release within the mildly acidic joint environment, whereas the latter facilitates precise mitochondrial targeting of our LNP@UA constructs. In this study, we used in vitro cellular and in vivo animal experiments to demonstrate that LNPs@UA effectively suppress macrophage and chondrocyte inflammation, scavenge ROS, promote mitochondrial autophagy, and mitigate ferroptosis. The results of transcriptomic sequencing indicated that LNPs@UA primarily modulates the NF-κB signaling pathway, thereby exerting a chondroprotective effect. This research underscores the potential use of LNPs@UA as a targeted therapeutic approach for OA, addressing key inflammatory pathways and offering promise for future clinical applications.

The chronic inflammatory milieu of OA is influenced by diverse factors. Recent research has highlighted the dysregulation of the M1/M2 macrophage ratio within synovial tissue, particularly the pivotal role of proinflammatory M1-type macrophages in driving the development of synovitis. While studies have demonstrated the anti-inflammatory properties of UA, its specific mechanism remains incompletely understood. In our investigation, we confirmed that LNPs@UA effectively inhibited M1-type macrophage polarization, attenuated inflammatory cytokine secretion, and concurrently promoted the differentiation of anti-inflammatory M2-type macrophages. This discovery provides a novel theoretical foundation for translating UA into clinical applications. The intra-articular inflammatory microenvironment accelerates chondrocyte damage and senescence. Increasing evidence underscores the critical role of mitophagy in protecting cartilage from OA-related degeneration [33]. Dysfunctional mitophagy significantly contributes to OA pathology [34], exacerbating ROS accumulation in chondrocytes during mitochondrial metabolism and thereby intensifying inflammation [20,21]. While ROS function as essential second messengers, their excess poses risks of oxidative damage. ROS accumulation in mitochondria disrupts mitochondrial structure and integrity, exacerbating cellular dysfunction [35]. Lin et al. demonstrated the potent ability of nitidine chloride to scavenge ROS effectively, thereby halting cellular senescence and alleviating inflammatory responses in OA [36]. Our study confirmed that LNPs@UA markedly reduce ROS levels in C28/I2 cells and demonstrate targeted affinity towards mitochondria, effectively mitigating LPS-induced structural damage. This targeted approach significantly decreases ROS release and enhances mitophagy levels, crucially mitigating mitochondrial dysfunction and associated pathologies. Furthermore, transcriptome sequencing analysis revealed that LNP@UA administration not only suppressed the NF-κB, TNF, and IL-17 signaling pathways but also activated pathways integral to eukaryotic ribosome biogenesis, base excision repair, DNA replication, nucleocytoplasmic transport, and other vital cellular processes. These findings suggest that LNP@UA exerts its anti-inflammatory effects by concurrently suppressing inflammatory signaling and enhancing cellular proliferation and repair mechanisms. The multifaceted protective actions of LNPs@UA highlight its potential application as a therapeutic candidate for addressing the complex pathophysiology of OA.

Furthermore, mitophagy plays a pivotal role as a trigger for cellular ferroptosis, a regulated form of cell death [37], with a dynamic interplay being observed between mitophagy and cellular ferroptosis [38]. Notably, Guo et al. demonstrated that deferoxamine, a chelating agent, inhibits ROS release and activates the Nrf2 signaling pathway, thereby suppressing cellular ferroptosis and suggesting a therapeutic approach for mitigating OA [39]. The capacity of mitochondrial autophagy to inhibit cellular iron death and related inflammatory responses has also been documented in studies of other inflammation-related diseases [40–42]. UA, which is recognized for its anti-inflammatory and antioxidant properties, has been shown to mitigate ferroptosis in LPS-induced acute lung injury in mice by enhancing the Keap1-Nrf2/HO-1 signaling cascade [43]. Our cutting-edge research demonstrated that LNPs@UA, a targeted delivery system harnessing the therapeutic potential of UA, effectively inhibited ferroptosis in both a murine osteoarthritis model and LPS-challenged chondrocytes. In vitro studies revealed that LNPs@UA upregulate key proteins (e.g., PINK1, Beclin1, Parkin, LC3-II, Nrf-2, SLC7A11, DHODH, HO-1, and GPX4) while concurrently suppressing ASCL4 and p62 levels and decreasing Fe^{2+} levels. This targeted modulation remodels the mitochondrial architecture, reduces ROS generation, and exerts potent antioxidant effects that attenuate ferroptosis. Therefore, we propose that LNPs@UA exert their effects on OA through multiple interconnected pathways, with complex interactions between them. We hypothesize that LNPs@UA targeting mitochondria may play a pivotal role in maintaining mitochondrial homeostasis, reducing ferroptosis by scavenging ROS [44], and potentially modulating macrophage polarization through these mechanisms [45,46]. However, the precise mechanisms involved remain to be fully elucidated, which represents a limitation of the current study. Further research will be needed to explore these interactions in greater detail in subsequent investigations. Compared with UA alone, LNPs@UA demonstrated enhanced antioxidant and anti-inflammatory capabilities, effectively suppressing ferroptosis through the modulation of the ROS/GPX4/HO-1 oxidation-antioxidation system. In vivo, LNPs@UA significantly reduced cartilage erosion and degeneration, increased COL-II expression, and decreased MMP-13 expression, highlighting their excellent chondroprotective effects. Further experiments confirmed that LNP@UA enhances mitophagy and inhibits ferroptosis in OA model mice. This innovative approach holds substantial promise for developing targeted therapies against conditions associated with ferroptosis.

In summary, advancements in drug delivery systems aim to optimize precision targeting, bioavailability, biosafety, manufacturing efficiency, and immunogenicity reduction. Our study leveraged microfluidic technology to synthesize LNPs@UA, incorporating Chol-TPP and 2-DIP-PEG as excipients in a one-step process. LNPs@UA exhibited low cytotoxicity, robust mitochondrial targeting efficiency in both cellular and animal models, and pH-responsive UA release within the acidic OA microenvironment. These nanoparticles effectively restored the mitochondrial ultrastructure, enhanced mitophagy, reduced ROS levels, and suppressed ferroptosis. Notably, LNPs@UA outperformed UA alone by promoting M2 macrophage polarization and inhibiting the NF-κB signaling pathway, thus mitigating inflammatory responses.

5. Conclusions

Collectively, our findings highlight the therapeutic potential use of LNPs@UA for managing OA, identifying it as a promising candidate for future clinical applications in treating this debilitating condition.

CRediT authorship contribution statement

Guoliang Yi: Writing – original draft, Methodology, Investigation. **Min Li:** Methodology, Investigation. **Jiayi Zhou:** Investigation. **Jinxin Li:** Data curation. **Xizheng Song:** Writing – review & editing, Funding acquisition. **Siming Li:** Writing – review & editing, Funding acquisition. **Jianghua Liu:** Writing – review & editing, Investigation, Conceptualization. **Haowei Zhang:** Writing – review & editing, Supervision, Conceptualization. **Zhiwei Chen:** Writing – review & editing, Supervision, Conceptualization.

Ethics approval statement

The University of South China Ethics Committee for Animal Experiment authorized all animal handling as being morally appropriate and ensured that it complied with any regulations (Approved number: 2023-253).

Consent for publication

Not applicable.

Funding

This work was supported by the National Natural Science Foundation of China (82472514, 81272055, 82272565), Scientific Research Project of Hunan Provincial Health Commission (202102080160), The outstanding youth program of Hunan Provincial Department of Education (23B0425), General Program of Hunan Provincial Health Commission (D202303068742), Hunan Natural Science Foundation (2022JJ30531), Clinical Medical Technology Innovation Guidance Program of Hunan Province (2021SK51821) and the Natural Science Foundation of Guangdong Province (2019A1515011085).

Declaration of competing interest

All the authors declare no conflict of interest.

Acknowledgements

Not applicable.

Abbreviations:

2-DIP	2-diisopropylamino ethylamine
ACLT	anterior cruciate ligament transection
ATP	adenosine triphosphatase
CLSM	confocal laser scanning microscope
COL-II	collagen type II
DLS	dynamic light scattering
EA	ellagic acid
ECM	extracellular matrix
FCM	flow cytometry
H&E	hematoxylin-eosin
IF	immunofluorescence
IHC	immunohistochemistry
LNPs	liposome nanoparticles
LPS	lipopolysaccharide
MMP	metalloproteinase
OA	osteoarthritis
PDI	polydispersity index
PEG	polyethylene glycol
ROS	reactive oxygen species
S&F	safranin o-fast green
TEM	transmission electron microscopy
TPP	triphenylphosphine
UA	urolithin A

Appendix A. Supplementary data

Supplementary data to this article can be found online at https://doi.org/10.1016/j.mtbio.2025.101697.

Data availability

Data will be made available on request.

References

[1] Q. Yao, X. Wu, C. Tao, W. Gong, M. Chen, M. Qu, Y. Zhong, T. He, S. Chen, G. Xiao, Osteoarthritis: pathogenic signaling pathways and therapeutic targets, Signal Transduct Target Ther 8 (1) (2023) 56.
[2] B. Gleason, E. Chisari, J. Parvizi, Osteoarthritis can also start in the gut: the gut-joint Axis, Indian J. Orthop. 56 (7) (2022) 1150–1155.
[3] R. Assi, J. Quintiens, S. Monteagudo, R.J. Lories, Innovation in targeted intra-articular therapies for osteoarthritis, Drugs 83 (8) (2023) 649–663.
[4] J. Yang, Y. Guo, S.M. Henning, B. Chan, J. Long, J. Zhong, R. Acin-Perez, A. Petcherski, O. Shirihai, D. Heber, Z. Li, Ellagic acid and its microbial metabolite urolithin A alleviate diet-induced insulin resistance in mice, Mol. Nutr. Food Res. 64 (19) (2020) e2000091.
[5] M. Zhang, S. Cui, B. Mao, Q. Zhang, J. Zhao, H. Zhang, X. Tang, W. Chen, Ellagic acid and intestinal microflora metabolite urolithin A: a review on its sources, metabolic distribution, health benefits, and biotransformation, Crit. Rev. Food Sci. Nutr. 63 (24) (2023) 6900–6922.
[6] J. Qiu, Y. Chen, J. Zhuo, L. Zhang, J. Liu, B. Wang, D. Sun, S. Yu, H. Lou, Urolithin A promotes mitophagy and suppresses NLRP3 inflammasome activation in lipopolysaccharide-induced BV2 microglial cells and MPTP-induced Parkinson's disease model, Neuropharmacology 207 (2022) 108963.
[7] H. Tao, W. Li, W. Zhang, C. Yang, C. Zhang, X. Liang, J. Yin, J. Bai, G. Ge, H. Zhang, X. Yang, H. Li, Y. Xu, Y. Hao, Y. Liu, D. Geng, Urolithin A suppresses RANKL-induced osteoclastogenesis and postmenopausal osteoporosis by, suppresses inflammation and downstream NF-κB activated pyroptosis pathways, Pharmacol. Res. 174 (2021) 105967.
[8] G. Cásedas, F. Les, C. Choya-Foces, M. Hugo, V. López, The metabolite urolithin-A ameliorates oxidative stress in neuro-2a cells, becoming a potential neuroprotective agent, Antioxidants 9 (2) (2020).
[9] P.Z. Shi, J.W. Wang, P.C. Wang, B. Han, X.H. Lu, Y.X. Ren, X.M. Feng, X.F. Cheng, L. Zhang, Urolithin a alleviates oxidative stress-induced senescence in nucleus pulposus-derived mesenchymal stem cells through SIRT1/PGC-1α pathway, World J. Stem Cell. 13 (12) (2021) 1928–1946.
[10] J. Lieberthal, N. Sambamurthy, C.R. Scanzello, Inflammation in joint injury and post-traumatic osteoarthritis, Osteoarthr. Cartil. 23 (11) (2015) 1825–1834.
[11] S.H. Kiaie, N. Majidi Zolbanin, A. Ahmadi, R. Bagherifar, H. Valizadeh, F. Kashanchi, R. Jafari, Recent advances in mRNA-LNP therapeutics: immunological and pharmacological aspects, J. Nanobiotechnol. 20 (1) (2022) 276.
[12] A.S. Reddy, B.A. Lakshmi, S. Kim, J. Kim, Synthesis and characterization of acetyl curcumin-loaded core/shell liposome nanoparticles via an electrospray process for drug delivery, and theranostic applications, Eur. J. Pharm. Biopharm. 142 (2019) 518–530, official journal of Arbeitsgemeinschaft fur Pharmazeutische Verfahrenstechnik e.V.
[13] E. Chiesa, R. Dorati, S. Pisani, B. Conti, G. Bergamini, T. Modena, I. Genta, The microfluidic technique and the manufacturing of polysaccharide nanoparticles, Pharmaceutics 10 (4) (2018).
[14] M. Sedighi, S. Sieber, F. Rahimi, M.A. Shahbazi, A.H. Rezayan, J. Huwyler, D. Witzigmann, Rapid optimization of liposome characteristics using a combined microfluidics and design-of-experiment approach, Drug delivery and translational research 9 (1) (2019) 404–413.
[15] V.M. Shah, C. Dorrell, A. Al-Fatease, B.L. Allen-Petersen, Y. Woo, Y. Bortnyak, R. Gheewala, B.C. Sheppard, R.C. Sears, A.W. Alani, Microfluidics formulated liposomes of hypoxia activated prodrug for treatment of pancreatic cancer, Pharmaceutics 14 (4) (2022).
[16] H. Shan, Q. Lin, D. Wang, X. Sun, B. Quan, X. Chen, Z. Chen, 3D printed integrated multi-layer microfluidic chips for ultra-high volumetric throughput nanoliposome preparation, Front. Bioeng. Biotechnol. 9 (2021) 773705.
[17] M. Zhang, W. Hu, C. Cai, Y. Wu, J. Li, S. Dong, Advanced application of stimuli-responsive drug delivery system for inflammatory arthritis treatment, Mater Today Bio 14 (2022) 100223.
[18] Y. Yan, A. Lu, Y. Dou, Z. Zhang, X.Y. Wang, L. Zhai, L.Y. Ai, M.Z. Du, L.X. Jiang, Y. J. Zhu, Y.J. Shi, X.Y. Liu, D. Jiang, J.C. Wang, Nanomedicines reprogram synovial macrophages by scavenging nitric oxide and silencing CA9 in progressive osteoarthritis, Adv. Sci. (2023) e2207490.
[19] Y. Wang, H. Jasper, S. Toan, D. Muid, X. Chang, H. Zhou, Mitophagy coordinates the mitochondrial unfolded protein response to attenuate inflammation-mediated myocardial injury, Redox Biol. 45 (2021) 102049.
[20] E. Park, S.W. Chung, ROS-mediated autophagy increases intracellular iron levels and ferroptosis by ferritin and transferrin receptor regulation, Cell Death Dis. 10 (11) (2019) 822.
[21] M. Zhao, Y. Wang, L. Li, S. Liu, C. Wang, Y. Yuan, G. Yang, Y. Chen, J. Cheng, Y. Lu, J. Liu, Mitochondrial ROS promote mitochondrial dysfunction and inflammation in ischemic acute kidney injury by disrupting TFAM-mediated mtDNA maintenance, Theranostics 11 (4) (2021) 1845–1863.
[22] Y. Shi, W. Bu, D. Chu, W. Lin, K. Li, X. Huang, X. Wang, Y. Wu, S. Wu, D. Li, Z. Xu, Z. Cao, H. Chen, H. Wang, Rescuing nucleus pulposus cells from ROS toxic microenvironment via mitochondria-targeted carbon dot-supported prussian blue to alleviate intervertebral disc degeneration, Adv. Healthcare Mater. 13 (8) (2024) e2303206.
[23] Y. Zhao, Y. Peng, Z. Yang, J. Lu, R. Li, Y. Shi, Y. Du, Z. Zhao, L. Hai, Y. Wu, pH-redox responsive cascade-targeted liposomes to intelligently deliver doxorubicin prodrugs and lonidamine for glioma, Eur. J. Med. Chem. 235 (2022) 114281.
[24] S. Li, X. Yang, Z. Feng, P. Wang, W. Zhu, S. Cui, Catalase enhances viability of human chondrocytes in culture by reducing reactive oxygen species and counteracting tumor necrosis factor-α-induced apoptosis, Cell. Physiol. Biochem. : international journal of experimental cellular physiology, biochemistry, and pharmacology 49 (6) (2018) 2427–2442.
[25] H. Li, Y. Yuan, L. Zhang, C. Xu, H. Xu, Z. Chen, Reprogramming macrophage polarization, depleting ROS by astaxanthin and thioketal-containing polymers delivering rapamycin for osteoarthritis treatment, Adv. Sci. 11 (9) (2024) e2305363.
[26] R. Han, Y. Liu, S. Li, X.J. Li, W. Yang, PINK1-PRKN mediated mitophagy: differences between in vitro and in vivo models, Autophagy 19 (5) (2023) 1396–1405.
[27] Y. Lu, Z. Li, S. Zhang, T. Zhang, Y. Liu, L. Zhang, Cellular mitophagy: mechanism, roles in diseases and small molecule pharmacological regulation, Theranostics 13 (2) (2023) 736–766.
[28] O. Zitka, S. Skalickova, J. Gumulec, M. Masarik, V. Adam, J. Hubalek, L. Trnkova, J. Kruseova, T. Eckschlager, R. Kizek, Redox status expressed as GSH:GSSG ratio as a marker for oxidative stress in paediatric tumour patients, Oncol. Lett. 4 (6) (2012) 1247–1253.
[29] Y. Miao, Y. Chen, F. Xue, K. Liu, B. Zhu, J. Gao, J. Yin, C. Zhang, G. Li, Contribution of ferroptosis and GPX4's dual functions to osteoarthritis progression, EBioMedicine 76 (2022) 103847.
[30] J. Xiao, C. Luo, A. Li, F. Cai, Y. Wang, X. Pan, L. Xu, Z. Wang, Z. Xing, L. Yu, Y. Chen, M. Tian, Icariin inhibits chondrocyte ferroptosis and alleviates osteoarthritis by enhancing the SLC7A11/GPX4 signaling, Int. Immunopharmacol. 133 (2024) 112010.
[31] H. Ruan, T. Zhu, T. Wang, Y. Guo, Y. Liu, J. Zheng, Quercetin modulates ferroptosis via the SIRT1/Nrf-2/HO-1 pathway and attenuates cartilage destruction in an osteoarthritis rat model, Int. J. Mol. Sci. 25 (13) (2024).
[32] Z. Yin, C. Qin, S. Pan, C. Shi, G. Wu, Y. Feng, J. Zhang, Z. Yu, B. Liang, J. Gui, Injectable hyperbranched PEG crosslinked hyaluronan hydrogel microparticles containing mir-99a-3p modified subcutaneous ADSCs-derived exosomes was

beneficial for long-term treatment of osteoarthritis, Mater Today Bio 23 (2023) 100813.
[33] K. Sun, X. Jing, J. Guo, X. Yao, F. Guo, Mitophagy in degenerative joint diseases, Autophagy 17 (9) (2021) 2082–2092.
[34] Z. Jin, B. Chang, Y. Wei, Y. Yang, H. Zhang, J. Liu, L. Piao, L. Bai, Curcumin exerts chondroprotective effects against osteoarthritis by promoting AMPK/PINK1/Parkin-mediated mitophagy, Biomedicine & pharmacotherapy = Biomedecine & pharmacotherapie 151 (2022) 113092.
[35] B. Wang, Y. Wang, J. Zhang, C. Hu, J. Jiang, Y. Li, Z. Peng, ROS-induced lipid peroxidation modulates cell death outcome: mechanisms behind apoptosis, autophagy, and ferroptosis, Arch. Toxicol. 97 (6) (2023) 1439–1451.
[36] C. Lin, L. Ge, L. Tang, Y. He, S.A.A. Moqbel, K. Xu, D. Ma, X. Zhou, J. Ran, L. Wu, Nitidine chloride alleviates inflammation and cellular senescence in murine osteoarthritis through scavenging ROS, Front. Pharmacol. 13 (2022) 919940.
[37] L. Su, J. Zhang, H. Gomez, J.A. Kellum, Z. Peng, Mitochondria ROS and mitophagy in acute kidney injury, Autophagy 19 (2) (2023) 401–414.
[38] C. Chu, X. Wang, C. Yang, F. Chen, L. Shi, W. Xu, K. Wang, B. Liu, C. Wang, D. Sun, W. Ding, Neutrophil extracellular traps drive intestinal microvascular endothelial ferroptosis by impairing Fundc1-dependent mitophagy, Redox Biol. 67 (2023) 102906.
[39] Z. Guo, J. Lin, K. Sun, J. Guo, X. Yao, G. Wang, L. Hou, J. Xu, J. Guo, F. Guo, Deferoxamine alleviates osteoarthritis by inhibiting chondrocyte ferroptosis and activating the Nrf2 pathway, Front. Pharmacol. 13 (2022) 791376.
[40] Q. Du, X. Wu, K. Ma, W. Liu, P. Liu, T. Hayashi, K. Mizuno, S. Hattori, H. Fujisaki, T. Ikejima, Silibinin alleviates ferroptosis of rat islet β cell INS-1 induced by the treatment with palmitic acid and high glucose through enhancing PINK1/parkin-mediated mitophagy, Arch. Biochem. Biophys. 743 (2023) 109644.
[41] Q. Lin, S. Li, H. Jin, H. Cai, X. Zhu, Y. Yang, J. Wu, C. Qi, X. Shao, J. Li, K. Zhang, W. Zhou, M. Zhang, J. Cheng, L. Gu, S. Mou, Z. Ni, Mitophagy alleviates cisplatin-induced renal tubular epithelial cell ferroptosis through ROS/HO-1/GPX4 axis, Int. J. Biol. Sci. 19 (4) (2023) 1192–1210.
[42] W.S. Yang, R. SriRamaratnam, M.E. Welsch, K. Shimada, R. Skouta, V. S. Viswanathan, J.H. Cheah, P.A. Clemons, A.F. Shamji, C.B. Clish, L.M. Brown, A. W. Girotti, V.W. Cornish, S.L. Schreiber, B.R. Stockwell, Regulation of ferroptotic cancer cell death by GPX4, Cell 156 (1–2) (2014) 317–331.
[43] L. Lou, M. Wang, J. He, S. Yang, F. Meng, S. Wang, X. Jin, J. Cai, C. Cai, Urolithin A (UA) attenuates ferroptosis in LPS-induced acute lung injury in mice by upregulating Keap1-Nrf2/HO-1 signaling pathway, Front. Pharmacol. 14 (2023) 1067402.
[44] B.R. Stockwell, Ferroptosis turns 10: emerging mechanisms, physiological functions, and therapeutic applications, Cell 185 (14) (2022) 2401–2421.
[45] E. Dai, L. Han, J. Liu, Y. Xie, G. Kroemer, D.J. Klionsky, H.J. Zeh, R. Kang, J. Wang, D. Tang, Autophagy-dependent ferroptosis drives tumor-associated macrophage polarization via release and uptake of oncogenic KRAS protein, Autophagy 16 (11) (2020) 2069–2083.
[46] A. Huang, Q. Li, X. Shi, J. Gao, Y. Ma, J. Ding, S. Hua, W. Zhou, An iron-containing nanomedicine for inducing deep tumor penetration and synergistic ferroptosis in enhanced pancreatic cancer therapy, Mater Today Bio 27 (2024) 101132.